

Isotope shifts and hyperfine splitting of the $^1S_0 \rightarrow ^3P_1$ transition in zinc

Felix Waldherr,* Lukas Möller, and Simon Stellmer
University of Bonn, Nussallee 12, 53115 Bonn, Germany
(Dated: May 29, 2026)

We report laser-induced-fluorescence spectroscopy of the $^1S_0 \rightarrow ^3P_1$ intercombination transition in neutral zinc at 307.6 nm. Isotope shifts are measured for all stable isotopes with kHz-level precision, improving previous data by about two orders of magnitude. For ^{67}Zn , we resolve the excited-state hyperfine structure and determine $\delta\nu_{\text{COG}}^{67,64} = 1085.933(4)$ MHz, $A = 608.922(1)$ MHz, and $B = -18.995(4)$ MHz. A King plot comparison with the $^1S_0 \rightarrow ^1P_1$ 214-nm transition results in field- and mass-shift parameters of $F_{307.6,214} = 1.17(5)$ and $K = -153(60)$ GHz u. These results provide the spectroscopic basis for narrow-line cooling and precision measurements based on zinc, including the development of an optical clock.

I. INTRODUCTION

Precision spectroscopy of atoms and molecules provides accurate frequency references and sensitive probes of atomic structure and provides the basis for tests of fundamental physics. A particularly successful class of systems is formed by alkaline-earth and alkaline-earth-like atoms, i.e. two-valence-electron atoms with a closed-shell 1S_0 ground state. This includes the group-II alkaline-earth atoms such as Mg, Ca, Sr, and Ba, as well as related alkaline-earth-like systems such as Zn, Cd, Hg, and Yb. Their level structure supports a diverse set of transitions: a broad singlet transition provides efficient first-stage cooling, while the narrow intercombination line enable second-stage cooling and high-resolution spectroscopy, ultimately leading to ultra-narrow clock transitions [1–4].

The isotope structure of these systems provides an additional degree of control. Bosonic isotopes with nuclear spin $I = 0$ have hyperfine-free spectra, while fermionic isotopes exhibit hyperfine structure and a weakly allowed $^1S_0 \rightarrow ^3P_0$ clock transition through hyperfine mixing [5]. This characteristic of simple bosonic spectra and richer fermionic structure is useful for experiments with laser-cooled atoms.

Neutral zinc is an attractive but less explored member of this alkaline-earth-like class. Laser cooling and trapping on the $^1S_0 \rightarrow ^1P_1$ transition at 214 nm have recently been demonstrated [6, 7]. Second-stage cooling of Zn requires isotope-resolved transition frequencies on the 307.6 nm intercombination line. This motivates a precise measurement of the isotope shifts and of the ^{67}Zn hyperfine structure.

Here, we present high-resolution laser-induced-fluorescence spectroscopy of the 307.6 nm intercombination line in a thermal beam of neutral zinc atoms. We determine isotope shifts for the stable isotopes relative to ^{64}Zn and resolve the excited-state hyperfine structure of ^{67}Zn . These measurements provide the frequency references needed for isotope-selective narrow-line cooling of zinc.

II. EXPERIMENTAL SETUP

Figure 1 shows a sketch of the experimental setup. A thermal beam of neutral Zn atoms is produced in a resistively heated oven operated at temperatures up to 400°C. The atomic beam defines the x axis and is collimated before entering the spectroscopy chamber by a 22 mm-long stainless-steel microtube array integrated into a heated blind flange, reducing the transverse velocity spread of the beam. From a Voigt fit to the Doppler-broadened spectrum, we obtain a transverse Doppler FWHM of $\Delta\nu_{\text{D}} = 155.2(5)$ MHz, corresponding to $\Delta v_{\perp} = \lambda\Delta\nu_{\text{D}} = 47.7(2)$ ms $^{-1}$. Interpreting this width as that of a one-dimensional Maxwellian velocity distribution gives an effective transverse temperature

$$T_{\perp} = \frac{m}{k_{\text{B}}} \left(\frac{\Delta v_{\perp}}{2\sqrt{2\ln 2}} \right)^2 \simeq 3.2 \text{ K}.$$

For an oven temperature of 400°C, the thermal mean velocity is $\bar{v} = \sqrt{8k_{\text{B}}T/(\pi m)} \simeq 466$ ms $^{-1}$. The measured transverse velocity width therefore corresponds to a full angular divergence of $\Delta\theta \simeq 2 \arctan[\Delta v_{\perp}/(2\bar{v})] = 5.9(1)^{\circ}$.

The spectroscopy light at 307.6 nm is generated by a commercial frequency-quadrupled diode-laser system (TOPTICA TA-FHG pro). The fundamental light near 1232 nm is stabilized to a home-built $L = 10$ cm reference cavity using the Pound–Drever–Hall locking scheme [8]. From a fitted cavity ring-down time of $\tau_{\text{cav}} = 22.131(7)$ μs , we infer a cavity linewidth of $\Delta\nu_{\text{cav}} = 1/(2\pi\tau_{\text{cav}}) = 7.191(2)$ kHz. Together with the measured free spectral range, this corresponds to a finesse of $\mathcal{F} = 208600(700)$. The laser frequency is monitored with a wavelength meter (HighFinesse WS8-10) at the second harmonic near 616 nm.

To improve the mode quality of the laser beam, the UV light is delivered to the experiment through a hydrogen-loaded photonic-crystal fiber (LMA-10 UV) [9]. We typically obtain a fiber-coupling efficiency of about 60%, allowing up to 8 mW of 307.6 nm light to be delivered to the apparatus. For the measurements reported here, we use $P \simeq 1.5$ mW in a beam with a $1/e^2$ diameter of approximately 6 mm. With $I_{\text{sat}} = \pi hc/(3\lambda^3\tau) \simeq 2.7 \times 10^{-2}$ mWcm $^{-2}$, this gives a saturation parameter of

* fwaldher@uni-bonn.de

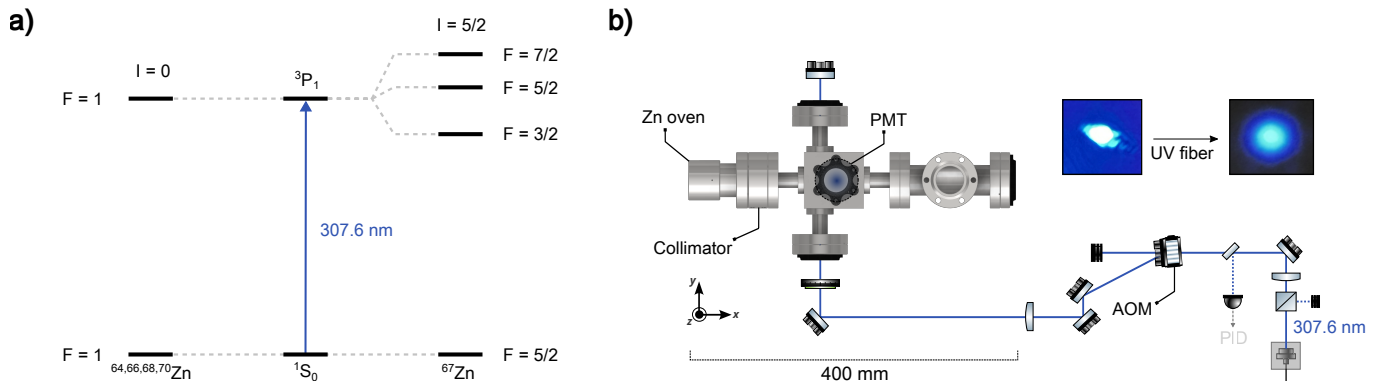


FIG. 1. Level structure and experimental setup for spectroscopy of the zinc intercombination line. (a) Relevant levels for the $^1S_0 \rightarrow ^3P_1$ transition at 307.6 nm, showing the hyperfine structure of ^{67}Zn . (b) Schematic of the atomic-beam fluorescence setup. Zn atoms from a thermal oven are collimated by a microtube array and interrogated by a retroreflected 307.6 nm spectroscopy beam. Fluorescence is detected along the z -direction with a photomultiplier tube (PMT).

$s_0 = I_0/I_{\text{sat}} \simeq 3.9 \times 10^2$, so that the transition is driven deeply into saturation.

After the fiber, the laser polarization is cleaned using a polarizing-beam-splitter cube and set with a half-wave plate. A small fraction of the polarization-cleaned beam is picked off with a wedged window and monitored on a photodiode for intensity stabilization. The spectroscopy beam then propagates along the y axis and intersects the atomic beam at right angles. The perpendicular alignment is first set using irises before and after the chamber and then refined by minimizing the offset between the Doppler-free feature and the center of the Doppler-broadened fluorescence envelope. To generate the Doppler-free signal, the beam is retroreflected after the vacuum chamber; the retroreflected light can be coupled back into the photonic-crystal fiber to verify spatial overlap.

During a scan, the frequency of the fundamental light is tuned by applying an offset to the cavity lock with an electro-optic modulator. This changes the frequency entering the nonlinear conversion stages. Since the light is subsequently frequency quadrupled to 307.6 nm, the applied scan is four times larger on the UV frequency axis. Throughout this work, all frequency intervals, linewidths, and scan steps are quoted on this UV scale. The isotope-shift spectra were recorded with a step size of 40 kHz in the UV.

Magnetic fields can be applied along the x and y axes using two independent pairs of coils. In the measurements discussed here, the relevant field is applied along x , parallel to the atomic beam, and defines the magnetic quantization axis. The spectroscopy light is linearly polarized parallel to this axis to drive predominantly π transitions. This polarization also favors fluorescence collection along the vertical z direction, since the dipole-emission pattern for π -polarized excitation has maximum emission perpendicular to the quantization axis.

Fluorescence is collected along z with a photomultiplier tube (PMT, Hamamatsu H9306). To suppress scattered light at the detector, the spectroscopy beam intersects the

atomic beam approximately 2 cm upstream of the PMT collection volume. At $\bar{v} \simeq 466 \text{ ms}^{-1}$, atoms traverse this distance in about 43 μs . With an excited-state lifetime of $\tau \simeq 26 \mu\text{s}$, roughly 19% of the excited atoms remain in the excited state until they reach the detection region. This spatial offset preserves a measurable fluorescence signal while efficiently rejecting prompt scattered light from the excitation region. For improved detection sensitivity, the spectroscopy light is amplitude-modulated with an acousto-optic modulator operated at a center frequency of $f_c = 200 \text{ MHz}$. The modulation frequency is $f_{\text{mod}} = 10 \text{ kHz}$, and the PMT signal is demodulated with a lock-in amplifier (MFLI, Zurich Instruments). With this detection scheme, even the weakest naturally abundant bosonic isotope, ^{70}Zn , is detected with a signal-to-noise ratio exceeding 10 after 10 s of averaging per frequency point.

III. RESULTS

Figure 2 shows the Doppler-broadened fluorescence spectrum of the $^1S_0 \rightarrow ^3P_1$ transition at 307.6 nm. On this scale, the observed line shape is dominated by the transverse velocity distribution of the thermal atomic beam. The relative amplitudes of the resolved components are consistent with the natural isotopic abundances [10], allowing the individual isotopes to be assigned in the Doppler-broadened spectrum. We describe the broad spectrum by a sum of Voigt profiles and use the fitted component positions as initial estimates for the isotope shifts. The Gaussian part of the Voigt profile represents residual transverse Doppler broadening, whereas the Lorentzian part contains the natural linewidth and additional homogeneous broadening, such as transit time broadening and saturation broadening.

For linearly polarized excitation, the detected fluorescence depends on the dipole emission pattern. For an even-mass isotope e , we follow Brown *et al.* [11] to model

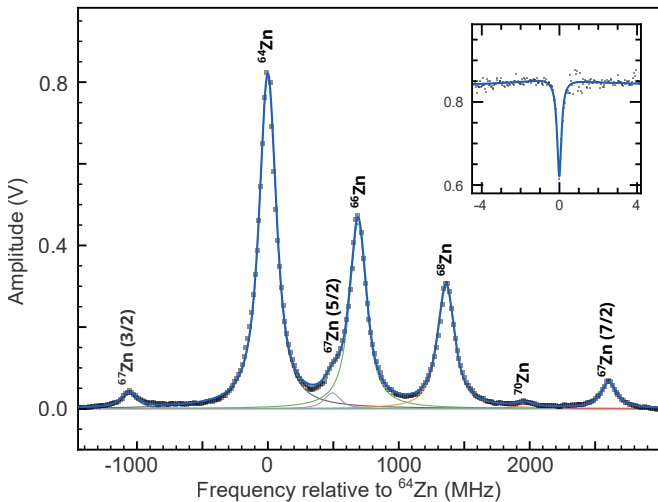


FIG. 2. Isotope-resolved fluorescence spectrum of the $^1S_0 \rightarrow ^3P_1$ transition in Zn at 307.6 nm. The main panel shows the Doppler-broadened spectrum, with the frequency axis referenced to the fitted ^{64}Zn resonance. The blue curve is a multi-Voigt fit including the bosonic isotopes and the three resolved ^{67}Zn hyperfine components, while the thin colored curves show the individual contributions. The inset shows a Doppler-free spectrum of the ^{64}Zn resonance used to determine the zero of the frequency axis.

the fluorescence signal as

$$S^{(e)}(\nu) = A_e V(\nu - \nu_e; \sigma_D, \gamma) [1 - P_2(\cos \theta) g(\theta_C)], \quad (1)$$

where A_e absorbs the isotope abundance, transition strength, and overall detection efficiency. The Voigt profile $V(\nu - \nu_e; \sigma_D, \gamma)$ is written explicitly as

$$\int_{-\infty}^{\infty} \frac{\exp[-\nu'^2/(2\sigma_D^2)]}{\sigma_D \sqrt{2\pi}} \frac{\gamma/\pi}{(\nu - \nu_e - \nu')^2 + \gamma^2} d\nu', \quad (2)$$

with Gaussian Doppler width σ_D and Lorentzian half-width γ . The angular factor is given by

$$P_2(\cos \theta) = \frac{3 \cos^2 \theta - 1}{2}, \quad g(\theta_C) = \cos \theta_C \cos^2 \left(\frac{\theta_C}{2} \right),$$

where θ is the angle between the excitation polarization and the detection direction, and θ_C is the half-angle of the finite collection cone. In our setup, a 2 inch collection lens is located about 60 mm from the fluorescence region, giving $\theta_C \simeq 23^\circ$. The PMT observes fluorescence perpendicular to the laser polarization, so that $\theta = \pi/2$. This geometry maximizes the detected fluorescence for the bosonic isotopes.

The same angular factor is applied to the fermionic isotope ^{67}Zn . In general, quantum-interference effects between different excitation pathways can modify fluorescence line shapes and their polarization dependence, as observed in related Zn spectroscopy measurements [6, 11]. In the present case, however, the $F' = 3/2, 5/2$, and $7/2$ hyperfine manifolds are well separated on the scale of the

linewidth, so spectral overlap between different manifolds is small. We therefore neglect interference between pathways belonging to different hyperfine states. Under this approximation, the detected fluorescence is maximized for excitation polarization perpendicular to the detection direction, as in the bosonic case [12].

A. Bosonic isotopes

The even mass number isotopes ^{64}Zn , ^{66}Zn , ^{68}Zn , and ^{70}Zn have nuclear spin $I = 0$ and no hyperfine structure. In the applied magnetic field of $B \simeq 340 \mu\text{T}$, corresponding to a coil current of 2 A, the σ^\pm ($\Delta m_J = \pm 1$) components are shifted away from the central π ($\Delta m_J = 0$) transition. With the spectroscopy polarization parallel to the field, we predominantly probe the π -transition, so each bosonic isotope contributes one fitted resonance for the isotope-shift analysis.

With the spectroscopy beam retroreflected, atoms with near-zero velocity along the laser axis interact with both counterpropagating beams, producing a Doppler-free saturation dip on top of the Doppler-broadened fluorescence background. The background-subtracted spectra of the bosonic isotopes are shown in Fig. 3.

The local spectrum is fitted with

$$S_{\text{DF}}^{(e)}(\nu) = S^{(e)}(\nu) - \frac{A_{\text{DF}}}{1 + 4(\nu - \nu_0)^2/\Gamma_{\text{DF}}^2}, \quad (3)$$

where $S^{(e)}(\nu)$ is the Voigt background from Eq. (1). The Lorentzian term describes the Doppler-free dip with center frequency ν_0 , FWHM Γ_{DF} , and amplitude A_{DF} . The fixed angular-emission factor is absorbed into A_{DF} .

B. Hyperfine structure of ^{67}Zn

For ^{67}Zn , the Doppler-free spectra resolve all three excited-state hyperfine manifolds of the $4s4p^3P_1$ state, $F' = 3/2, 5/2$, and $7/2$, as shown in Fig. 4. Under a magnetic field of $B \simeq 340 \mu\text{T}$ applied along the x -axis, the Zeeman structure is resolved as well. The center-of-gravity (COG) isotope shift is obtained from the degeneracy-weighted average over the three hyperfine manifolds,

$$\nu_{\text{COG}} = \frac{\sum_{F'} (2F' + 1) \nu_{F'}}{\sum_{F'} (2F' + 1)} = \frac{4\nu_{3/2} + 6\nu_{5/2} + 8\nu_{7/2}}{18}.$$

The observed hyperfine-component frequencies can be written as

$$\nu_{F'} = \nu_{\text{COG}} + \Delta\nu_{F'},$$

where ν_{COG} is the fine-structure center-of-gravity frequency and $\Delta\nu_{F'}$ are the hyperfine shifts. The latter are given by the Casimir formula

$$\Delta\nu_{F'} = \frac{1}{2}AK + B \frac{\frac{3}{4}K(K+1) - I(I+1)J(J+1)}{2I(2I-1)J(2J-1)},$$

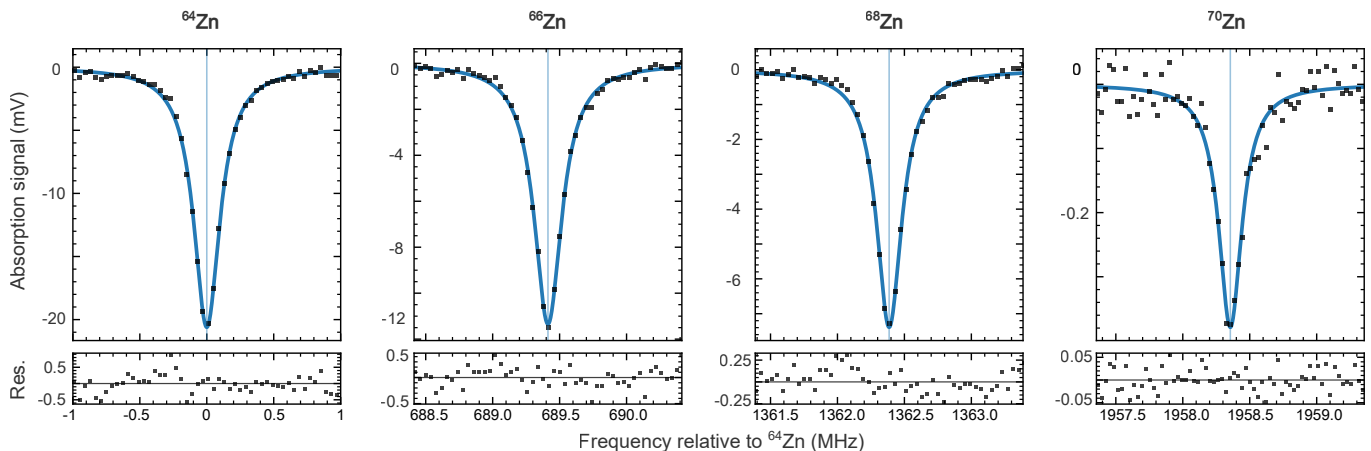


FIG. 3. Doppler-free spectra of the bosonic zinc isotopes on the $^1S_0 \rightarrow ^3P_1$ transition at 307.6 nm. Each panel shows the background-subtracted fluorescence signal, with the frequency axis referenced to the ^{64}Zn resonance. Black points are the measured data and blue curves are Lorentzian fits to the saturation dips. The lower panels show the corresponding fit residuals. The fitted centers are used to determine the isotope shifts of ^{66}Zn , ^{68}Zn , and ^{70}Zn relative to ^{64}Zn .

where

$$K = F'(F' + 1) - I(I + 1) - J(J + 1).$$

For ^{67}Zn , the nuclear spin is $I = 5/2$. In the excited 3P_1 state, the electronic angular momentum is $J = 1$. Taking differences between the Casimir shifts gives

$$\nu_{5/2-3/2} = \Delta\nu_{5/2} - \Delta\nu_{3/2} = \frac{5}{2}A - \frac{3}{2}B,$$

$$\nu_{7/2-5/2} = \Delta\nu_{7/2} - \Delta\nu_{5/2} = \frac{7}{2}A + \frac{21}{20}B.$$

The extracted intervals, COG shifts, and hyperfine constants A and B are listed in Table I.

TABLE I. Hyperfine intervals, hyperfine constants, and center-of-gravity (COG) isotope shifts for the ^{67}Zn $4s4p^3P_1$ state. Uncertainties in parentheses are statistical fit uncertainties.

Quantity	This work MHz	Previous measurement MHz
Measured hyperfine intervals		
$\nu_{5/2-3/2}$	1550.795(7)	1551.565(4) ^a
$\nu_{7/2-5/2}$	2111.283(6)	2111.300(3) ^a
Extracted hyperfine constants		
$A(^3P_1)$	608.922(1)	609.086(1) ^a
$B(^3P_1)$	-18.995(4)	-18.782(8) ^a
Center-of-gravity isotope shifts		
$\delta\nu_{\text{COG}}^{67,64}$	1085.933(3)	1085.7(2.0) ^b
$\delta\nu_{\text{COG}}^{67,66}$	396.522(3)	397.1(2.0) ^b

^aOptical double-resonance measurement by Byron *et al.* [13].

^bAtomic-beam measurement by Campbell *et al.* [14].

The measured hyperfine constants also provide useful benchmarks for atomic-structure theory [15]. Mul-

ticonfiguration Hartree-Fock (MCHF) and multiconfiguration Dirac-Hartree-Fock (MCDHF) calculations of the $4s4p^3P_{1,2}$ states have been used to extract the ^{67}Zn nuclear quadrupole moment from experimental hyperfine constants and calculated electric-field gradients [16]. Because the magnetic-dipole and electric-quadrupole constants are strongly correlated, small changes in the fitted hyperfine intervals or in the theoretical treatment of electron correlation, relativistic effects, and spin polarization can produce appreciable deviations in A and B . The present kHz-level values for the $4s4p^3P_1$ state therefore provide an additional constraint for future many-body calculations of Zn I [17].

C. Isotope shift analysis

Isotope shifts reflect the fact that different isotopes have different nuclear masses and charge distributions. The mass difference changes the electronic transition energy through the normal and specific mass shifts, while the change in nuclear charge radius gives rise to the field shift. The total isotope shift is therefore commonly written as the sum of a mass-shift and a field-shift contribution,

$$\delta\nu^{A,64} = K \left(\frac{1}{m_A} - \frac{1}{m_{64}} \right) + F\delta\langle r^2 \rangle^{A,64},$$

where m_A denotes the mass of the isotope with mass number A , K and F are the mass- and field-shift constants of the transition. Table II summarizes the isotope shifts measured for the stable zinc isotopes on the $^1S_0 \rightarrow ^3P_1$ transition. For each isotope pair, the resonance frequencies were obtained from interleaved measurements of ^{64}Zn and the target isotope. This sequence reduces sensitivity to slow drifts of the experiment, particularly of the reference cavity. For the bosonic isotopes, the isotope shift is obtained directly from the difference between the

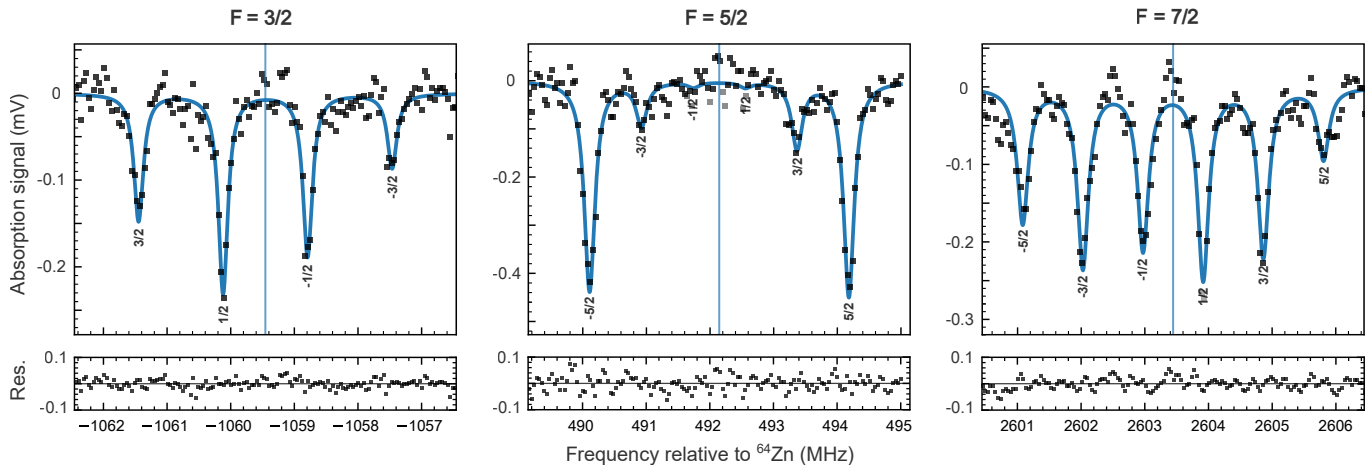


FIG. 4. Doppler-free spectra of the three resolved hyperfine manifolds of ^{67}Zn . The frequency axis is referenced to the ^{64}Zn resonance. Blue markers indicate the fitted line positions used to determine the hyperfine intervals and the degeneracy-weighted center-of-gravity isotope shift.

TABLE II. Summary of the isotope-shift measurements of the zinc $^1S_0 \rightarrow ^3P_1$ transition at 307.6 nm. For ^{67}Zn , the center-of-gravity (COG) isotope shift is listed.

Quantity	This work MHz	Previous measurement MHz
$\delta\nu^{66,64}$	689.411(3)	688.6(1.0) ^a
$\delta\nu^{67,64}$	1085.933(4)	1085.7(2.2) ^a
$\delta\nu^{68,64}$	1362.390(3)	1365.2(1.4) ^a
$\delta\nu^{70,64}$	1958.358(7)	1962.2(1.7) ^a

^a Atomic-beam measurement by Campbell *et al.* [14].

fitted Doppler-free resonance positions. For ^{67}Zn , the individual hyperfine components were measured separately. The isotope shift of the fermionic isotope is therefore reported as the center-of-gravity shift. The same data also yield the excited-state hyperfine intervals and the corresponding magnetic-dipole and electric-quadrupole hyperfine constants. The residual drift of the experimental setup during each interleaved measurement sequence was determined from the time dependence of the repeated ^{64}Zn reference measurements and subtracted from the extracted isotope shifts. The size of this correction, together with the uncertainty assigned to the remaining uncompensated drift, is discussed in Sec. III D. This procedure allows the isotope shifts to be determined largely independently of the absolute cavity drift over the full measurement time.

To compare the present 307.6 nm isotope shifts with the previously measured $^1S_0 \rightarrow ^1P_1$ transition at 214 nm [6], we construct a King plot. Isotope shifts contain both mass-shift and field-shift contributions; comparing two transitions allows these contributions to be tested for mutual consistency. For each isotope pair we define the

modified isotope shift

$$m\delta\nu^{A,64} = \frac{\delta\nu^{A,64}}{\mu^{A,64}}, \quad \mu^{A,64} = \frac{1}{m_A} - \frac{1}{m_{64}}. \quad (4)$$

If the mass- and field-shift terms describe the data, the modified isotope shifts of the two transitions obey a linear relation,

$$m\delta\nu_{307.6}^{A,64} = K + F_{307.6,214} m\delta\nu_{214}^{A,64}, \quad (5)$$

where the slope gives the relative field-shift factor and the intercept gives the relative mass-shift offset. We fit the 307.6 nm and 214 nm modified isotope shifts using orthogonal distance regression. The resulting linear fit and its 1σ confidence band are shown in Fig. 5. From the fit we obtain

$$F_{307.6,214} = 1.17(5), \quad K = -153(60) \text{ GHz u.}$$

The near-unity slope reflects the common 1S_0 ground state of both transitions [6], and the observed linearity shows consistency of the two isotope-shift data sets within the present uncertainties.

D. Systematic effects and residual uncertainties

We evaluate the corrections applied to the measured isotope shifts and the residual uncertainty from the dominant systematic effects. The resulting uncertainty budget is summarized in Table III.

a. Reference-cavity drift The reference cavity operates at the fundamental wavelength, but all drift rates are quoted on the UV frequency axis after frequency quadrupling. On this scale, the thermal cavity drift can reach about 2 kHz/min. Since the isotope shifts are measured in an interleaved sequence, the common linear drift largely cancels between neighboring isotope scans. The relevant

TABLE III. Uncertainty budget for the isotope-shift measurements of the zinc $^1S_0 \rightarrow ^3P_1$ transition at 307.6 nm. The common contributions are applied to all pairs of isotopes, while the geometry term is isotope-dependent because it arises from mass-dependent velocity-class selection. Statistical and systematic contributions are added in quadrature to obtain the final uncertainties.

Contribution	$^{64}\text{Zn}-^{66}\text{Zn}$ kHz	$^{64}\text{Zn}-^{67}\text{Zn}$ kHz	$^{64}\text{Zn}-^{68}\text{Zn}$ kHz	$^{64}\text{Zn}-^{70}\text{Zn}$ kHz
Common systematic contributions				
Reference-cavity drift			1.0	
Intensity dependence			1.9	
Lock-point shifts			negligible	
B -field dependence			negligible	
Oven-temperature dependence			negligible	
Common systematic subtotal			2.1	
Isotope-dependent systematic contribution				
Geometry / velocity-class selection	1.3	2.0	2.6	3.8
Total systematic uncertainty	2.5	2.9	3.4	4.4
Statistical uncertainty	1.5	2.6	0.7	6.0
Final uncertainty	2.9	3.9	3.4	7.4

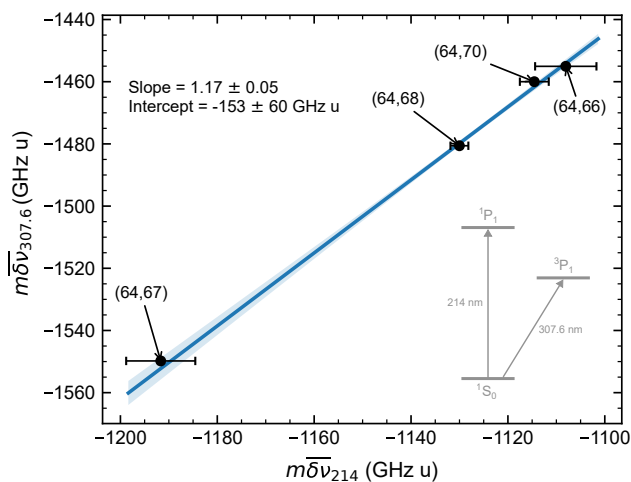


FIG. 5. King plot comparing the modified isotope shifts of the $^1S_0 \rightarrow ^3P_1$ transition at 307.6 nm with those of the $^1S_0 \rightarrow ^1P_1$ transition at 214 nm [6]. Each point corresponds to one isotope pair relative to ^{64}Zn . The blue line shows a linear fit and the shaded band indicates the 1σ confidence interval of the fit. The inset shows the two electronic transitions used in the comparison.

contribution is therefore the uncertainty of the fitted drift slope, which we determine to be below 0.05 kHz/min. For a typical isotope-pair measurement duration of 20 min, this gives a residual uncertainty of 1.0 kHz.

b. Intensity dependence Intensity-dependent line-center shifts were characterized by repeating ^{64}Zn measurements at different laser powers. The observed dependence may include AC Stark shifts as well as intensity-dependent line-shape effects from saturation, optical pumping, or residual asymmetries of the Doppler-free signal. A linear fit gives an empirical coefficient of $\beta_P = 27.3(7)$ kHz/mW. With a power stability of 50 μW ,

the corresponding uncertainty for an isotope-shift pair is

$$\sigma_P = \sqrt{2}\beta_P\Delta P = 1.93 \text{ kHz.}$$

c. Instability of the lock point For each isotope change, the EOM frequency is changed and the laser is relocked to the reference cavity. A change of the lock point, for example due to an electronic offset of the PDH error signal or a slightly different relocking condition, would therefore appear as an additional frequency offset between isotope scans. We tested this by repeatedly measuring the ^{64}Zn resonance with the cavity lock kept continuously engaged and after intentionally relocking the laser between successive scans. No systematic difference between the two data sets is observed within the statistical scatter of the fitted line centers. We therefore apply no lock-point correction and bound this contribution to be negligible at the present level of precision.

d. Zeeman shift Residual magnetic-field effects were tested by repeating the interleaved $^{64}\text{Zn}-^{66}\text{Zn}$ isotope-shift measurement for different applied x -field currents. We find a small current dependence of 2.1(2) kHz/A. For the actual measurements, the relevant current mismatch between interleaved isotope scans is only $\Delta I \simeq 1$ mA, giving a residual shift of 0.002 kHz.

e. Oven-temperature Possible oven-temperature-dependent shifts were tested by repeating the interleaved $^{64}\text{Zn}-^{66}\text{Zn}$ isotope-shift measurement at 411°C and 430°C. No change was observed within the experimental uncertainty.

f. Velocity-class selection A residual angular mismatch between the forward and retroreflected spectroscopy beams can make the Doppler-free signal sensitive to a selected transverse velocity class rather than to the center of the Doppler-broadened velocity distribution. We observe that the horizontal alignment of the retroreflection mirror has a strong influence on the line shape: intentional misalignment changes the asymmetry and quality of the Doppler-free feature and shifts

the fitted line center. We quantify this effect by deliberately changing the retroreflection angle with a micrometer screw over a range of ± 3 mrad. A linear fit to the measured line-center shifts gives an alignment sensitivity of approximately $\frac{\partial\nu}{\partial\theta} \simeq 3.1 \times 10^2$ kHz/mrad.

During normal measurements the retroreflected beam was recoupled into the photonic-crystal fiber after propagation over approximately 2 m. The coupling efficiency was stable to within about 10%. For a Gaussian mode with mode-field diameter $8.4 \mu\text{m}$, a 10% coupling loss corresponds to a transverse mode mismatch of order $1\text{--}2 \mu\text{m}$ at the fiber input. Since the coupling lens partly converts angular deviations into position at the fiber, we do not use this as an exact pointing measurement. Instead, we take the full mode-field diameter as a conservative upper bound on the effective beam displacement, corresponding to $\delta\theta \simeq \frac{8.4 \mu\text{m}}{2 \text{ m}} = 4.2 \mu\text{rad}$. Applying the measured alignment sensitivity to this angular scale gives $\sigma_{\text{geom}}^{66,64} \simeq \delta\theta \cdot \frac{\partial\nu}{\partial\theta} \simeq 1.3$ kHz. Since this effect is tied to the selected transverse velocity class, we scale it with the thermal velocity dependence $v_{\perp} \propto m^{-1/2}$,

$$\sigma_{\text{geom}}^{A,64} = \sigma_{\text{geom}}^{66,64} \frac{|1 - \sqrt{64/A}|}{|1 - \sqrt{64/66}|},$$

using the $^{64}\text{Zn}\text{--}^{66}\text{Zn}$ pair as the reference.

The total systematic uncertainty for each isotope pair is obtained by adding the common systematic subtotal and the isotope-dependent geometry term in quadrature. The final uncertainty is then obtained by adding this systematic uncertainty and the statistical fit uncertainty in quadrature.

IV. CONCLUSION & DISCUSSION

We have performed high-resolution spectroscopy of the $^1S_0 \rightarrow ^3P_1$ intercombination line in neutral zinc using laser-induced fluorescence from a thermal atomic beam. Isotope shifts for all stable isotopes were measured relative to ^{64}Zn using interleaved scan sequences, in which repeated measurements of the reference isotope were used

to correct the drift of the experimental setup. The shifts were measured with kHz-level precision, improving the accuracy of the available 307.6 nm isotope-shift data by about two orders of magnitude.

For the bosonic isotopes, the measured shifts are consistent with previous work while providing substantially smaller uncertainties. For the fermionic isotope ^{67}Zn , the resolved $F' = 3/2, 5/2,$ and $7/2$ hyperfine manifolds allow us to determine the center-of-gravity isotope shift and to extract the magnetic-dipole and electric-quadrupole hyperfine constants of the $4s4p^3P_1$ state. The observed deviations of the extracted A and B constants from previous values are small on the MHz scale, but significant compared with the quoted kHz-level uncertainties, and therefore deserve further investigation with independent measurements.

The present results provide a precise reference data set for the zinc intercombination line. This is a useful step toward implementing and characterizing second-stage cooling on this narrow transition, and more generally toward improving the control of high precision zinc experiments. In combination with isotope shifts on other transitions, the data also enable King plot consistency checks of mass- and field-shift contributions. A particularly interesting future target is the ultra-narrow $^1S_0 \rightarrow ^3P_0$ clock transition, which would provide an additional optical transition for King plot comparisons.

ACKNOWLEDGMENTS

We acknowledge funding from Deutsche Forschungsgemeinschaft DFG through grants INST 217/978-1 FUGG and 496941189, as well as through the Cluster of Excellence "ML4Q" (EXC 2004/1 – 390534769) and from the European Commission through project 101080164 "UVQUANT". We thank D. Röser for early experimental work, and F. Wolf from PTB for providing us with the UV fiber. We thank the entire team of the UVQUANT consortium for inspiring discussions and technical advice. Data underlying the results presented in this paper are not publicly available at this time, but may be obtained from the authors upon reasonable request.

-
- [1] M. Witkowski, G. Kowzan, R. Munoz-Rodriguez, R. Ciuryło, P. S. Żuchowski, P. Masłowski, and M. Zawada, Absolute frequency and isotope shift measurements of mercury $^1S_0 \rightarrow ^3P_1$ transition, *Opt. Express* **27**, 11069 (2019).
 - [2] M. Gu, K. Koenigsmann, J. Yang, and P. Schauss, Modulation transfer spectroscopy and isotope shifts of the $^1S_0 \rightarrow ^3P_1$ transition of ytterbium, *Phys. Rev. A* **112**, 062807 (2025).
 - [3] H. Miyake, N. C. Pisenti, P. K. Elgee, A. Sitaram, and G. K. Campbell, Isotope-shift spectroscopy of the $^1S_0 \rightarrow ^3P_1$ and $^1S_0 \rightarrow ^3P_0$ transitions in strontium, *Phys. Rev. Res.* **1**, 033113 (2019).
 - [4] M. G. Tarallo, T. Mazzoni, N. Poli, D. V. Sutyryn, X. Zhang, and G. M. Tino, Test of Einstein equivalence principle for 0-spin and half-integer-spin atoms: Search for spin-gravity coupling effects, *Phys. Rev. Lett.* **113**, 023005 (2014).
 - [5] A. Aeppli, K. Kim, W. Warfield, M. S. Safronova, and J. Ye, Clock with 8×10^{-19} systematic uncertainty, *Phys. Rev. Lett.* **133**, 023401 (2024).
 - [6] D. Röser, J. E. Padilla-Castillo, B. Ohayon, R. Thomas, S. Truppe, G. Meijer, S. Stellmer, and S. C. Wright, Hyperfine structure and isotope shifts of the $(4s^2)^1S_0 \rightarrow$

- ($4s4p$) 1P_1 transition in atomic zinc, *Phys. Rev. A* **109**, 012806 (2024).
- [7] L. Möller and S. Stellmer, Magneto-optical trapping of zinc (2025), arXiv:2510.21376 [physics.atom-ph].
- [8] R. W. P. Drever, J. L. Hall, F. V. Kowalski, J. Hough, G. M. Ford, A. J. Munley, and H. Ward, Laser phase and frequency stabilization using an optical resonator, *Appl. Phys. B* **31**, 97 (1983).
- [9] Y. Colombe, D. H. Slichter, A. C. Wilson, D. Leibfried, and D. J. Wineland, Single-mode optical fiber for high-power, low-loss UV transmission, *Opt. Express* **22**, 19783 (2014).
- [10] K. J. R. Rosman and P. D. P. Taylor, Isotopic compositions of the elements 1997, *Pure Appl. Chem.* **70**, 217 (1998).
- [11] R. C. Brown, S. Wu, J. V. Porto, C. J. Sansonetti, C. E. Simien, S. M. Brewer, J. N. Tan, and J. D. Gillaspay, Quantum interference and light polarization effects in unresolvable atomic lines: Application to a precise measurement of the $^{6,7}\text{Li}$ D_2 lines, *Phys. Rev. A* **87**, 032504 (2013).
- [12] S. Hofsäss, J. E. Padilla-Castillo, S. C. Wright, S. Kray, R. Thomas, B. G. Sartakov, B. Ohayon, G. Meijer, and S. Truppe, High-resolution isotope-shift spectroscopy of Cd I, *Phys. Rev. Res.* **5**, 013043 (2023).
- [13] F. W. Byron, M. N. McDermott, R. Novick, B. W. Perry, and E. B. Saloman, Spin and nuclear moments of 245-day ^{65}Zn ; redetermination of the hfs of ^{67}Zn and $\tau(^3P_1)$ of zinc, *Phys. Rev.* **134**, A47 (1964).
- [14] P. Campbell, J. Billowes, and I. S. Grant, The specific mass shift of the zinc atomic ground state, *J. Phys. B* **30**, 2351 (1997).
- [15] B. K. Sahoo and B. Ohayon, All-optical differential radii in zinc, *Phys. Rev. Res.* **5**, 043142 (2023).
- [16] J. Bieroń, L. Filippin, G. Gaigalas, M. Godefroid, P. Jönsson, and P. Pyykkö, Ab initio calculations of the hyperfine structure of zinc and evaluation of the nuclear quadrupole moment $Q(^{67}\text{Zn})$, *Phys. Rev. A* **97**, 062505 (2018).
- [17] L. Filippin, J. Bieroń, G. Gaigalas, M. Godefroid, and P. Jönsson, Multiconfiguration calculations of electronic isotope-shift factors in Zn I, *Phys. Rev. A* **96**, 042502 (2017).